nature communications

Article

https://doi.org/10.1038/s41467-024-51732-9

Flexible solid-liquid bi-continuous electrically and thermally conductive nanocomposite for electromagnetic interference shielding and heat dissipation

Received: 4 February 2024

Accepted: 14 August 2024

Published online: 06 September 2024

Check for updates

Yue Sun[1], Yunting Su[1], Ziyuan Chai[1], Lei Jiang[1] & Liping Heng[1]

In the era of 5 G, the rise in power density in miniaturized, flexible electronic devices has created an urgent need for thin, flexible, polymer-based electrically and thermally conductive nanocomposites to address challenges related to electromagnetic interference (EMI) and heat accumulation. However, the difficulties in establishing enduring and continuous transfer pathways for electrons and phonons using solid-rigid conductive fillers within insulative polymer matrices limit the development of such nanocomposites. Herein, we incorporate MXene-bridging-liquid metal (MBLM) solid-liquid bi-continuous electrical-thermal conductive networks within aramid nanofiber/polyvinyl alcohol (AP) matrices, resulting in the AP/MBLM nanocomposite with ultra-high electrical conductivity (3984 S/cm) and distinguished thermal conductivity of 13.17 W m^{-1} K^{-1}. This nanocomposite exhibits excellent EMI shielding efficiency (*SE*) of 74.6 dB at a minimal thickness of 22 μm, and maintains high EMI shielding stability after enduring various harsh conditions. Meanwhile, the AP/MBLM nanocomposite also demonstrates promising heat dissipation behavior. This work expands the concept of creating thin films with high electrical and thermal conductivity.

The 21st century has witnessed significant advancements in modern electronic devices and communication techniques. In the era of 5 G, the trends toward miniaturization and flexibility of the next-generation electronic systems are undeniable[1]. However, the miniaturization and high integration of electronic devices have escalated power density, consequently exacerbating challenges related to electromagnetic interference (EMI) and heat accumulation. These challenges have detrimental impacts on the safe operation of the entire electric system and human health[2–5], posing threats to the reliability and working life of electronics[6–9]. For the engagement of these challenges, and considering the extremely limited space in the miniaturized flexible electronics[10,11], thin flexible films with dual capabilities of EMI shielding and heat dissipation, tailored for modern electronic systems are urgently demanded[12].

The synergy of high electrical and thermal conductivity is the key to the development of bifunctional materials capable of both EMI shielding and heat dissipation. The integration of solid, rigid conductive fillers with flexible polymer matrices has proven to be an effective approach in developing flexible electrical/thermal conductive films[13,14]. For this purpose, various solid conductive fillers with different dimensionalities, such as Ag nanoparticles[15], Ag nanowires[16], carbon nanotubes (CNT)[17,18], graphene nanosheets[19–22], and two-dimensional (2D) transition-metal carbides or nitrides (MXene)[23–28], etc., have been incorporated with polymer. For instance, Wang et al.

[1]Key Laboratory of Bio-Inspired Smart Interfacial Science and Technology of Ministry of Education, School of Chemistry, Beihang University, Beijing 100191, PR China. e-mail: henglp@buaa.edu.cn

prepared a graphene nanoplatelet (GNP)/nylon composite paper with an electrical conductivity of 24.3 S/cm exhibited a high EMI shielding efficiency (*SE*) of 58.1 dB at a thickness of 180 μm[29], along with a high thermal conductivity of 15.8 W m^{-1} K^{-1}, and a tensile strength of 31 MPa. Gu's group demonstrated the fabrication of a flexible Fe_3O_4/MXene/polyimide film with an excellent electrical conductivity of 280 S/cm and an *EMI SE* of 85 dB at a thickness of 75 μm[26]. Additionally, this nanocomposite showed a high thermal conductivity of 3.49 W m^{-1} K^{-1} and a tensile strength of 65.3 MPa. However, the structural robustness of the material is inadequate for ensuring prolonged durability. To address this frailty, nanofibers with promising mechanical strength were employed as matrices[30–34]. Particularly aramid nanofiber (ANF), known for its exceptional mechanical properties and thermal endurance[35,36]. For instance, a robust MXene/ANF nanocomposite film, created through vacuum-assisted filtration (VAF)[25], displayed notable properties: a tensile strength of 230.5 MPa, an electrical conductivity of 913 S/cm, a high *EMI SE* of 53.5 dB at 28 μm thickness, and an in-plane thermal conductivity of 0.43 W m^{-1} K^{-1}. In addition, a magnetic MXene/FeNi/ANF nanocomposite film prepared via VAF with a tensile strength of 113.4 MPa demonstrated an electrical conductivity of 26.7 S/cm[37], a high *EMI SE* of 60.7 dB at a thickness of 50 μm, and a thermal conductivity of 4.72 W m^{-1} K^{-1}. Despite efforts, the EMI specific shielding efficiency (*SSE*) per unit thickness for current materials remains suboptimal, and the thermal conductivity is insufficient, typically below 1000 dB/mm and 10 W m^{-1} K^{-1}, respectively (Supplementary Table 1). This primarily stems from the difficulties faced by solid electrical/thermal conductive fillers in establishing fully continuous conductive pathways for charge and thermal carriers like electrons and phonons within insulative polymer matrices, owing to factors such as insufficient orientation of solid fillers and cage effect generated by surrounding nanofibers[38,39]. To address these challenges, a high-filling rate is often employed. However, due to the rigidity of the solid fillers, this approach may result in a loss of flexibility, and the continuity of the conductive pathways becomes vulnerable to external forces, particularly under harsh conditions. Generally speaking, pursuing the concurrent achievement of high-performance EMI shielding and heat dissipation in ultra-thin, robust and flexible film with harsh condition endurance poses a challenging endeavor.

Herein, we constructed layered MXene-bridging-liquid metal (MBLM) solid-liquid bi-continuous electrical and thermal conductive networks in ANF/polyvinyl alcohol (PVA) (AP) matrices via a scalable sol-gel-film conversion approach and following hot-pressing process. The AP/MBLM nanocomposite exhibits an ultra-high electrical conductivity of 3984 S/cm and a high thermal conductivity of 13.17 W m^{-1} K^{-1}. Consequently, the AP/MBLM film achieves a promising *EMI SE* of 74.6 dB at a small thickness of 22 μm, with the maximum EMI *SSE* per unit thickness reaching up to 4950 dB/mm. The AP/MBLM films demonstrate notable EMI shielding stability after enduring harsh conditions (*EMI SE* maintains above 70 dB after 10000 bending cycles; 1000 folding cycles; ultrasonication for 1 h; liquid nitrogen soaking for 1 h; 200 °C treatment for 24 h, or 400 °C treatment for 1 h, respectively. *EMI SE* remains at a high value of 61 dB even after direct burning for 60 s). Furthermore, the AP/MBLM nanocomposite film exhibits effective heat dissipation performance as a thermal interface material (TIM). The AP/MBLM films also demonstrate promising robustness, with maximum tensile strength and toughness reaching 253.3 MPa and 14.1 MJ/m^3, respectively. This work introduces a strategy for constructing solid-liquid bi-continuous conductive networks in fiber-based composites. This approach holds the potential for scalable fabrication of highly electrically and thermally conductive films, suitable for high-performance EMI shielding and effective thermal management in miniaturized flexible electronics.

Results

Fabrication strategy and characterization of AP/MBLM nanocomposite film

To construct solid-liquid bi-continuous conductive networks in ANF matrices for flexible films with high electrical and thermal conductivity. Eutectic gallium indium (EGaIn) liquid metal (LM) with intriguing room-temperature fluidity, exceptional electrical and thermal conductivity[40–43], was employed as the liquid component of the conductive network. 2D MXene nanosheets with excellent electrical and thermal conductivity were chosen as the solid component[4,28]. As shown in Fig. 1a, the fluid LM welds the MXene nanosheets interspersed in the ANF matrices. Simultaneously, the MXene nanosheets spatially confine the LM and mutually bridged resulting in the formation of layered MBLM solid-liquid bi-continuous conductive networks within ANF supporting matrices. These interconnected networks establish ultrafast transfer pathways for electrons and phonons among the MXene nanosheets and LM lamellae, mitigating the adverse cage effect of the insulative ANF matrices on the overall electrical and thermal conductivity of the nanocomposite[39]. To achieve a homogeneous distribution of LM in ANF matrices, a stable negatively charged sodium alginate (SA)-covered-LM (SA@LM)/DMSO nano-emulsion with a mean diameter of 330 nm was obtained through tip-sonication (Fig. 1b, Supplementary Fig. 1 and Supplementary Fig. 2). The electrostatic repulsion forces between the SA@LM nanodroplets counteracts gravity, ensuring a stable dispersion[44,45]. $Ti_3C_2T_x$ (MXene) nanosheets with a mean lateral size of 4.76 μm and lateral height of 1.3 nm were prepared through selective etching and exfoliation of the Ti_3AlC_2 MAX phase (Fig. 1c, d and Supplementary Fig. 3a–d). The nanosheets were subsequently dispersed in DMSO (Supplementary Fig. 3e). ANF with diameters ranging from 9 to 19 nm and lengths of several micrometers were prepared through the exfoliation of short-cut Kevlar macro fibers in DMSO/KOH system (Fig. 1e and Supplementary Fig. 4a–e). To enhance the mechanical properties of the nanocomposite, hydroxyl-rich short-chain PVA was added to the ANF/DMSO dispersion as an interfacial reinforcing agent[46,47], simultaneously it assembled with the ANF chains forming AP/DMSO dispersion (Supplementary Fig. 4f). A homogenous colloidal dispersion is achieved by mixing the SA@LM/DMSO nano-emulsion with the MXene/DMSO dispersion and the AP/DMSO dispersion. The homogeneous dispersity of the mixture was confirmed by the Tyndall effect generated by a laser beam and through the measurement of zeta-potential (Supplementary Fig. 2 and Supplementary Fig. 5). Figure 1f schematically illustrates a continuous fabrication process of the large-area AP/MBLM film. The homogeneous colloidal dispersion was initially blade-coated on a PET substrate and then underwent a sol-gel conversion process in deionized (DI) water, attributed to the reprotonation of the ANF[25,48], consequently, an AP/MXene/SA@LM composite hydrogel is formed (Supplementary Fig. 6). Subsequently, the hydrogel was transferred into a mixture of tert-butylalcohol and DI water (mass ratio of 1:1) for extraction for 24 h and then the hydrogel was evaporated to form AP/MXene/SA@LM heterogenous film with all the component densely packed, yet the SA@LM remained isolated from each other. Ultimately, following hot-pressing, the SA@LM nanodroplets ruptured, allowing its inner bulk to flow out adhering and welding the MXene nanosheets, this can be verified through the shifts of zeta-potential (Supplementary Fig. 2). This transformation resulted in the establishment of a layered MBLM solid-liquid bi-continuous conductive network. Following these processes, large-area AP/MBLM films measuring 10.5 cm × 23 cm with good flexibility were prepared (Supplementary Fig. 7). As illustrated in Fig. 1g and Supplementary Fig. 8, the AP/MBLM nanocomposite film outperforms other recently reported materials tailored for EMI shielding and heat dissipation, including various aspects of electrical and thermal conductivity, total *EMI SE*, *EMI SSE*, tensile strength, and area.

https://doi.org/10.1038/s41467-024-51732-9

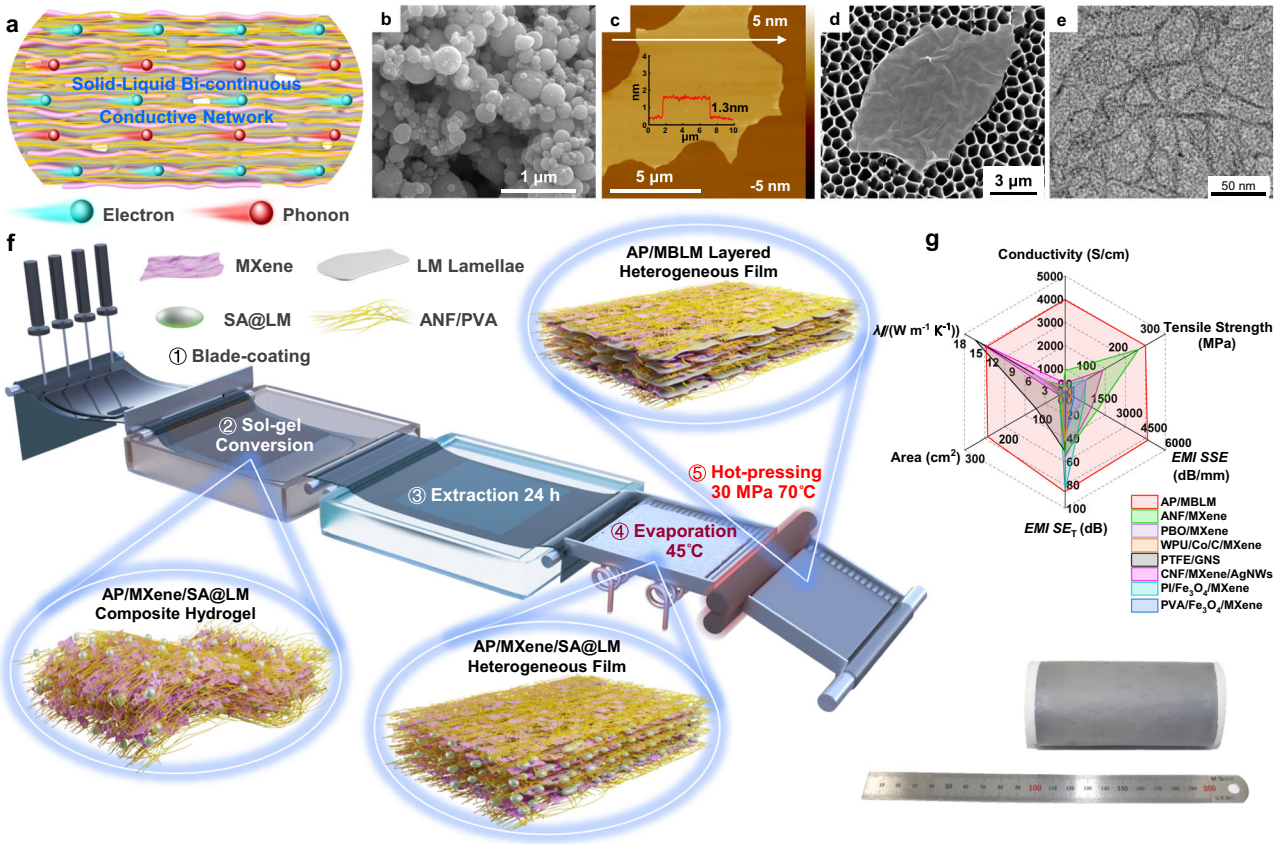

Fig. 1 | Fabrication strategy of the AP/MBLM nanocomposite film. a Schematic illustration of the MXene-bridging-liquid metal (MBLM) solid-liquid bi-continuous thermally and electrically conductive network. **b** SEM image of the sodium alginate (SA)-covered-LM nanoparticles. **c** AFM image (inset: lateral height data) of the MXene nanosheet. **d** SEM image of the MXene nanosheet. **e** TEM image of the aramid nanofibers. **f** Schematic illustration of the fabrication strategy of the ANF/polyvinyl alcohol (AP)/MBLM film and a large-area AP/MBLM film rolled on a scroll. **g** Radar phase diagram of performance comparison for AP/MBLM film with other recently reported composite films with dual functionalities of EMI shielding and heat dissipation (details can be found in Supplementary Fig. 8a and Supplementary Table 1).

To characterize the formation of the solid-liquid bi-continuous networks in the AP/MBLM nanocomposite film, the cross-sectional morphology was initially observed. In the AP/MXene/SA@LM hydrogel, the SA@LM nanodroplets were orbicular (Supplementary Fig. 9). After the evaporation process, the LM nanodroplets in the AP/MXene/SA@LM film were partially sintered, exhibiting an ellipsoidal shape (Fig. 2a). This transformation was influenced by the synergistic effects of gravity, capillary forces derived from the liquid bridge of the nanofibers, and evaporation[45,49], along with the interaction forces including hydrogen bonds and electrostatic forces formed among the AP matrices, MXene nanosheets and SA@LM nanodroplets[49,50]. As shown in Fig. 2b, following the mechanical sintering process, the thickness of the AP/MBLM film reduced from 20 μm to approximately 16 μm. During the hot-pressing process, the partially sintered SA@LM droplets were ruptured, and their inner bulk flowed and spread out across the AP matrix. The flowed LM sintered together among the MXene nanosheets, mutually bridged and forming a layered heterogenous solid-liquid bi-continuous network. This can be validated by the distribution of representative elements of C, N, Ga, and Ti in the cross-section of the AP/MBLM film (Fig. 2b) and the surface morphology of the films (Fig. 2c) after the mechanical sintering process. The extrusion of LM and the formation of LM lamellae result in a highly dense inner structure within the AP/MBLM film. The porosity of the AP/MBLM film, obtained by using the ratio of void volume to material volume derived from Nano X-ray computed tomography (CT), is only 3.25% (Supplementary Fig. 10). X-ray photoelectron spectroscopy (XPS) is depicted in Fig. 2d, showcasing characteristic peaks of Ti 2*p* and F 1*s* for MXene nanosheets in the spectrum of the AP/MBLM film. The intensities of these peaks are noticeably weakened due to the coverage of ANF[39]. Additionally, N 1*s* peak for ANF, as well as the Ga 2*p*, and Ga 3*d* peaks for EGaIn LM can also be observed at their corresponding binding energies in the AP/MBLM nanocomposite[23,51]. These observations confirm the successful integration of MXene nanosheets, LM lamellae, and AP matrices. Raman spectra of the AP/MBLM film (Supplementary Fig. 11) further prove the successful combination of MXene nanosheets and AP matrices[35,52]. The high-resolution XPS spectra of Ga 3*d*, Ga 2*p*, and In 3*d* in the AP/MBLM film (Supplementary Fig. 12) substantiate the presence of elemental gallium and indium, along with their respective oxides in the nanocomposite[51,53]. Specifically, the high-resolution XPS spectra of In 3*d* exhibits an orbital overlap, further confirming the combination of LM and MXene in the AP/MBLM nanocomposite. The C 1*s* high-resolution XPS spectra (Fig. 2e) show the presence of the C-N bond related to ANF in the AP/MBLM film[23]. As shown in O 1*s* spectra (Fig. 2f), the characteristic peaks of Ti-O, C-Ti-O_x, Ti-OH, and C = O appear in both the MXene and AP/MBLM films[33]. The shift in the binding energy of the Ti-OH characteristic peak from 532.1 eV to 531.9 eV reveals the formation of hydrogen-bonds among MXene nanosheets and the polymer components of PVA, ANF and SA[25]. As shown in Fig. 2g, diffraction peaks corresponding to the (002) plane of MXene and the (110) plane of ANF are discernible in the XRD pattern of AP/MBLM nanocomposite[52]. The (002) peak of the AP/MBLM nanocomposite shifts to a lower angle compared with pure MXene due to the increase in lattice spacing, providing evidence for the successful integration of MXene

https://doi.org/10.1038/s41467-024-51732-9

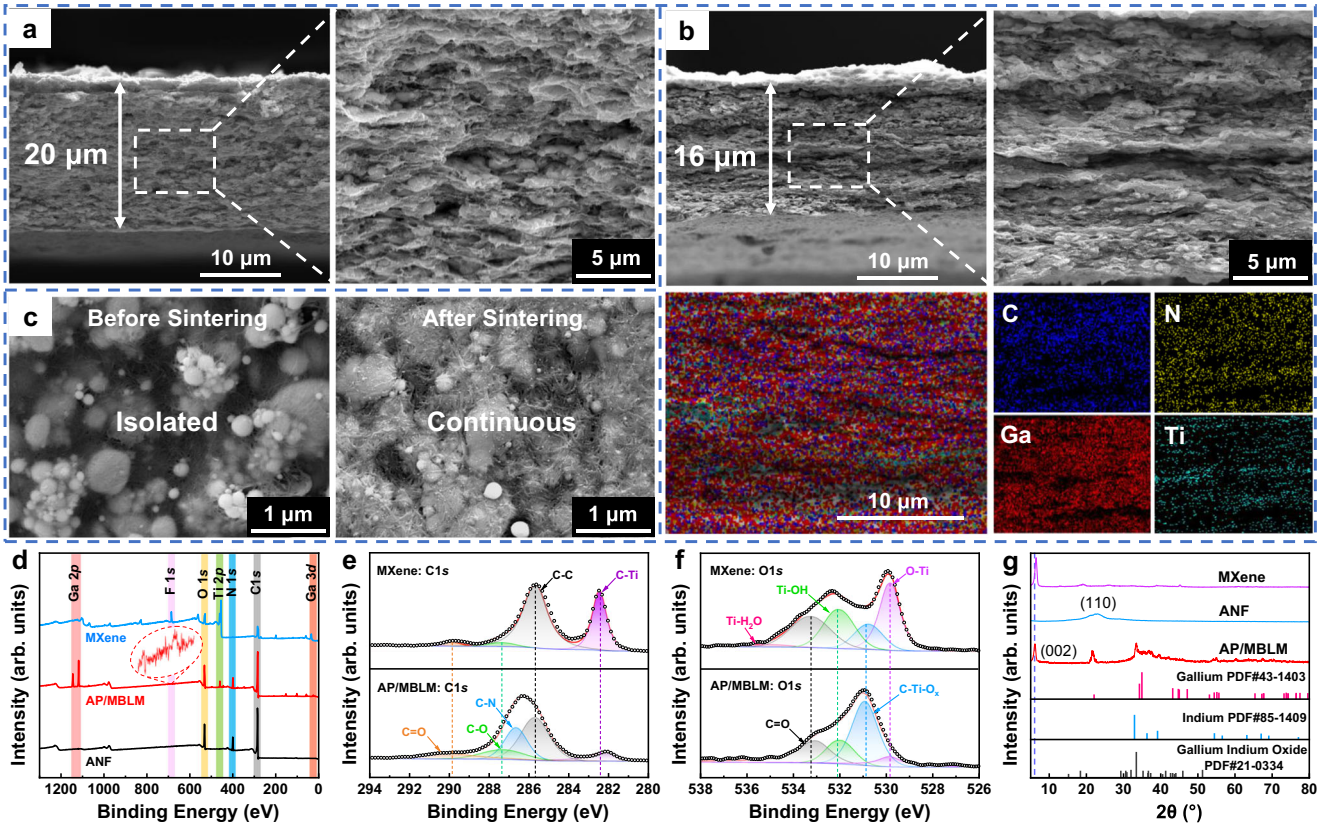

Fig. 2 | Structure and chemistry characterization of AP/MBLM nanocomposite film. a Cross-section SEM images of the evaporated ANF/polyvinyl alcohol (AP)/MXene/sodium alginate-covered-liquid metal (SA@LM) film. **b** SEM images and EDS element mappings in the cross-section of the AP/MXene-bridging-liquid metal (MBLM) film. **c** Surface SEM images of AP/MBLM films before and after sintering. **d** XPS full spectrum of ANF, MXene, and AP/MBLM film, the inset part of the AP/MBLM film spectrum is the high-resolution XPS spectrum of F1*s*. High-resolution XPS spectrum of **e** C 1*s*, **f** O 1*s* for the AP/MBLM film and MXene. **g** XRD patterns of MXene, ANF, AP/MBLM film, and standard PDF cards of Ga, In, and Ga_2O_3/In_2O_3.

nanosheets with AP matrices[33]. Additionally, the diffraction peaks associated with the EGaIn LM in AP/MBLM nanocomposite closely align with the standard PDF cards of gallium, indium, and gallium indium oxide[51,54].

Electrical properties and EMI shielding performance

The EMI shielding performance typically exhibits a positive correlation with the electrical conductivity of the material[4,55]. As shown in Fig. 3a, the mechanical sintering of the LM droplets leads to a substantial increase in electrical conductivity. The electrical conductivity of the AP/MBLM film increases with a higher LM weight ratio attributing to the maturation of the solid-liquid bi-continuous conductive network (Supplementary Fig. 13), and the value of the AP/MBLM11 nanocomposite film reaching a notable value of 3984 S/cm. However, since a solid-liquid bi-continuous conductive network has already been established in the AP/MBLM11 film, the electrical conductivity of the AP/MBLM13 film only marginally increases to 4265 S/cm with a further increase in LM content[56]. Notably, MXene nanosheets play a crucial role in bridging the LM lamellae. The electrical conductivity of composite films lacking MXene nanosheets (AP/LM) is significantly lower than that of AP/MBLM films with the same LM weight ratio (Fig. 3b). Specifically, the electrical conductivity of the AP/MBLM11 film (3984 S/cm) is 5.4 times higher than that of the AP/LM11 film (733 S/cm). The cross-section of the AP/LM11 film reveals a distinct separation of LM by the insulative ANF, resulting in cage effect that leads to the unsatisfactory electrical conductivity[39] (Supplementary Fig. 14). We conducted finite element simulations to verify the observed discrepancy in electrical conductivity in the composite films attributed to the presence of MXene nanosheets. 2D models based on the microstructure obtained from SEM images were built (Supplementary Fig. 15). In the simulation, one side of the 2D model is grounded and the current density through the other side is constantly set at 5 A m^{-2}. Figure 3c shows the simulation results of the electrical potential distribution of AP/MBLM and AP/LM films. As the color shifts from pink to blue, there is a consistent and monotonic increase in electrical potential. A pronounced color gradient indicates a heightened resistance of the film. It is evident that the color gradient of the AP/MBLM film is smaller than that of the AP/LM film, signifying a lower resistivity in the AP/MBLM film[54], which is consistent with the experimental results.

The exceptional electrical conductivity renders the AP/MBLM film highly suitable for EMI shielding. Consequently, we examined the EMI shielding performance of the AP/MBLM film using the waveguide method. Figure 4a illustrates the EMI shielding performance evaluated for AP/LM and AP/MBLM films across various LM weight ratios; The *EMI SE* of the AP/MBLM films consistently surpasses the values of the AP/LM films across all LM weight ratios, and far beyond the value of the AP/MXene film and AP film without any conductive filler. Specifically, the *EMI SE* of the AP/MBLM11 film reaches 74.6 dB, whereas the AP/LM11 film only achieves a value of 48.4 dB. However, with the limited increase in electrical conductivity, the *EMI SE* of the AP/MBLM13 film only increases by 2.1 dB compared to the AP/MBLM11 film. As shown in Fig. 4b and Supplementary Fig. 16, the overall *EMI SE* of the AP/MBLM films shows a stable fluctuation in the whole frequency range of the X-band. The total EMI shielding effectiveness (SE_T) of a material can be divided into reflection effectiveness (SE_R) and absorption effectiveness (SE_A)[57]. As shown in Fig. 4c, the SE_R and the SE_A value of the AP/MBLM film increase monotonically with the increase in LM weight ratio, and the SE_R and SE_A value of the AP/MBLM11 film reaches the high value of

https://doi.org/10.1038/s41467-024-51732-9

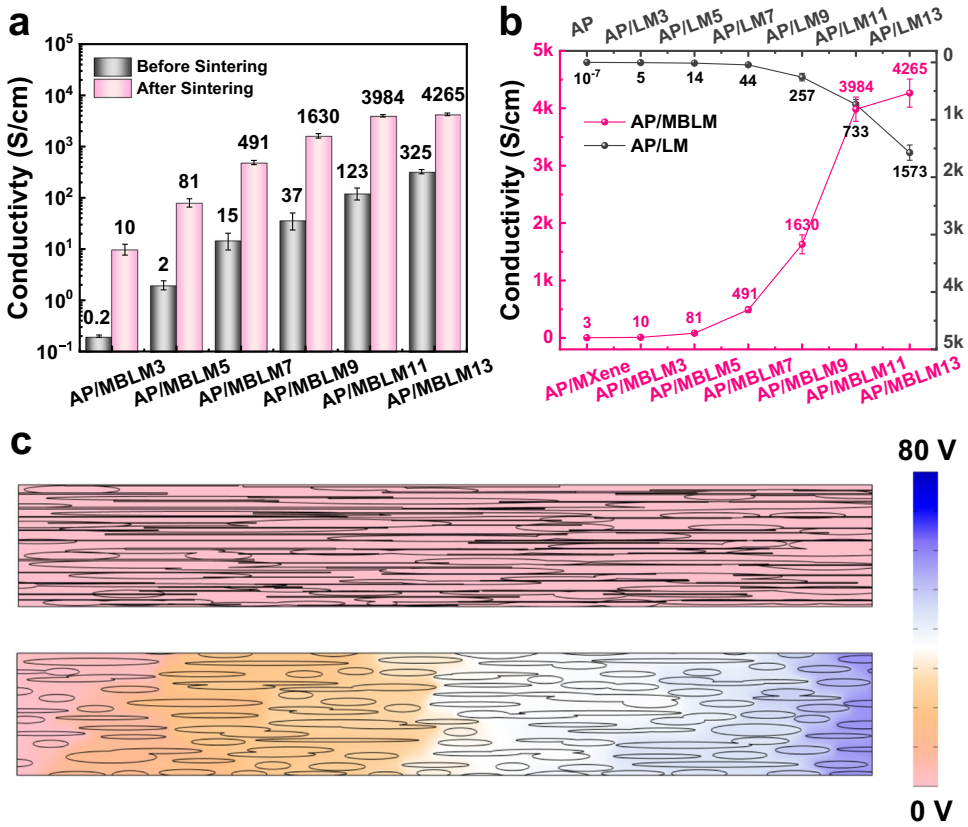

Fig. 3 | Electrical properties of AP/MBLM nanocomposite films. a Electrical conductivity of ANF/polyvinyl alcohol (AP)/ MXene-bridging-liquid metal (MBLM) films before and after mechanical sintering. **b** Electrical conductivity of AP/MBLM films and AP/LM films. The error bars (**a**, **b**) represent the standard deviations of the measured values ($n = 5$). **c** Finite element simulation results of X-directional electrical potential distribution of AP/MBLM and AP/LM films.

18.6 dB and 56.0 dB respectively. For the analysis of the EMI shielding mechanism and to comprehend the trend in *EMI SE* variation, the average values of reflectivity (R), absorptivity (A), and transmissivity (T) coefficients of the AP/MBLM film over the X-band frequency are shown in Fig. 4d. According to the conservation of energy, $R + A + T = 1$[57]. The R-value exhibits an ascending trend with the increase in LM weight ratio, reaching 0.982 for the AP/MBLM13 film, in contrast to 0.743 for the AP/MXene film. It is noteworthy that although the values of SE_A are consistently higher than those of SE_R in all samples, the R coefficient values are consistently higher than the A coefficient values. This is because the reflection of the EM wave occurs prior to absorption, and there is a logarithmic relationship between SE_R and the R coefficient ($R > 0.5$ when $SE_R > 3$ dB)[57]. Consequently, the EMI shielding mechanism of the AP/MBLM film is dominated by reflection, a consequence of its ultra-high electrical conductance[57]. Figure 4e illustrates the EMI shielding mechanism of the AP/MBLM film. Firstly, the major part of the incident electromagnetic (EM) wave is reflected at the interface among the surface of AP/MBLM nanocomposite and air due to the large impedance mismatch[31]. Subsequently, since the T value is very close to 0 (Fig. 4d), the penetrated EM wave entering the inner structure of the AP/MBLM film mostly dissipates attributed to the following effects: Firstly, internal multiple reflections and scattering occur within the numerous heterogeneous interfaces between MXene nanosheets, LM lamellae and AP matrices due to the impedance mismatch between these components. This prolongs the transmission paths of the EM wave and enhances EM wave absorption[51,57]; Secondly, ohmic losses arise as a substantial induced current is generated through the interaction of the penetrated EM wave with the high-density charge carriers (electrons and holes) within the MBLM solid-liquid bi-continuous conductive networks, converting EM energy into thermal energy[58,59]; Thirdly, polarization relaxation loss arises through the following mechanisms: When the nanocomposite is exposed to an alternating EM field, due to the discrepancy in the moving speed and polarization reaction rate of charge carriers in different dielectric materials, the accumulation of free charges occurs at the interfaces between MXene/AP matrices, LM/AP matrices, and MXene/LM, causing interfacial polarizaition[24,60]. According to the Maxwell-Wagner-Sillars polarization principle[61,62], the layered structure and the numerous interfaces, synergizing with the large conductivity mismatch among LM, MXene and the AP matrices, amplify charge storage capacity and enhance interfacial polarization. Furthermore, local diploes generate at the defects of the etched MXene nanosheets and between Ti and the electronegative terminal groups (—F, =O, and —OH) on its surface, resulting in dipole polarization[4]. Both forms of polarization contribute to polarization relaxation loss under alternating EM fields[58,60]. To validate the enhancement of *EMI SE* stemming from the aforementioned effects within the inner structure of the nanocomposite film, further investigations were conducted. The *EMI SE* of AP/MBLM films with different thicknesses were tested (Supplementary Fig. 17), and the results reveal a monotonical increasing tendency in *EMI SE* with the augmentation of thickness (Fig. 4f, Supplementary Fig. 18 and Supplementary Table 1), a promising *EMI SE* of 85.5 dB is reached at a thickness of 31 μm, and the *EMI SSE* per unit thickness reached an ultra-high value of 4950 dB/mm at the thickness of 12 μm. Subsequently, the average theoretically calculated *EMI SE* of a homogeneous EMI shielding film was obtained by applying frequencies (f, MHz) within the X-band range, along with the thickness (t, cm) and conductivity (σ, S/cm) identical to the AP/MBLM11 films to Simon's formula as shown in Eq. 1. The theoretically calculated *EMI SE* (SE_{theo}) was compared with the experimentally

https://doi.org/10.1038/s41467-024-51732-9

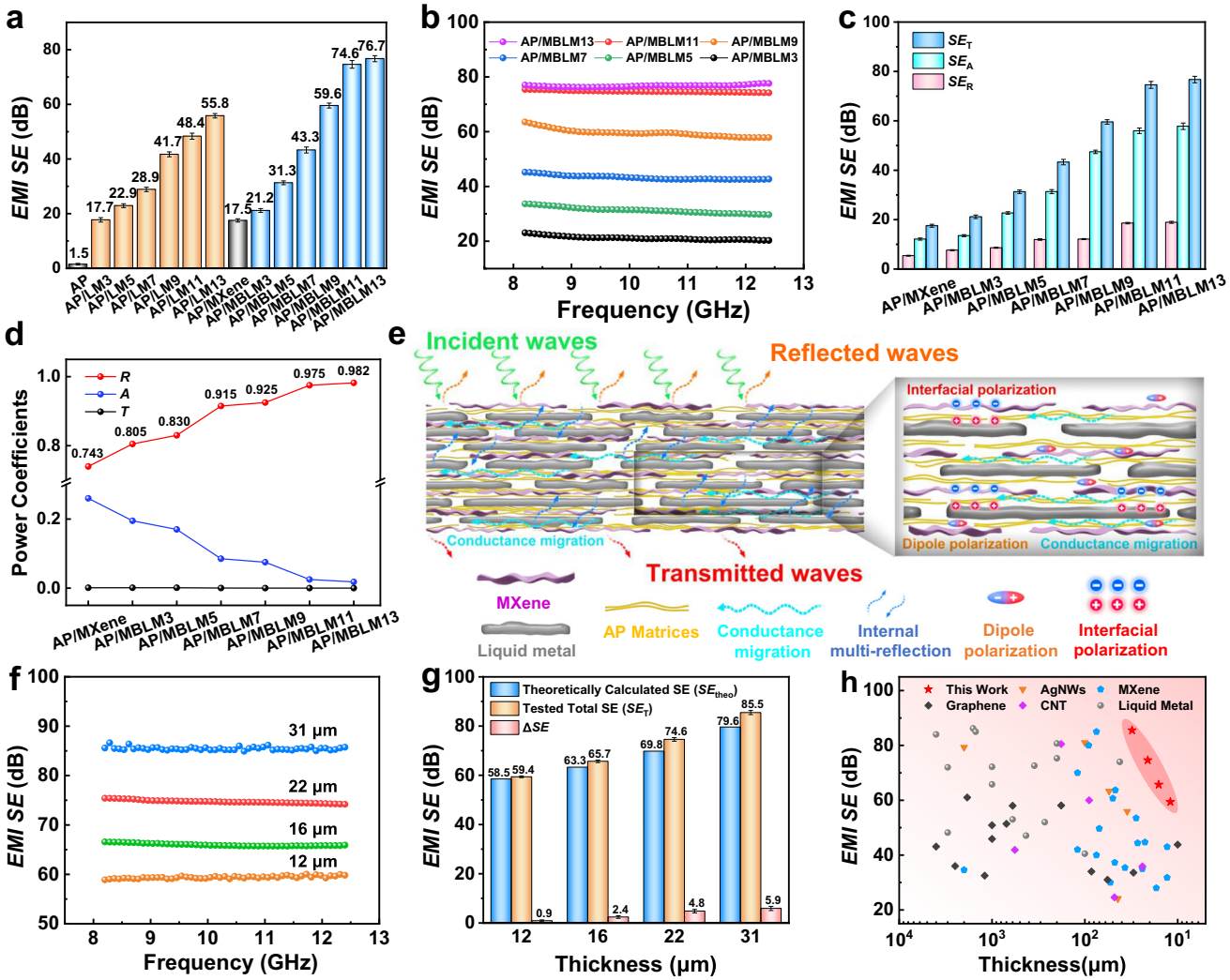

Fig. 4 | Electromagnetic interference shielding performance and mechanism of AP/MBLM nanocomposite films. a X-band EMI shielding efficiency (*SE*) of ANF/PVA (AP) film, AP/MXene film and AP/LM, AP/MXene-bridging-liquid metal (MBLM) films across various LM weight ratios at a thickness of approximately 22 μm. Error bars represent standard deviations. **b** *EMI SE* curves over the frequency range of 8.2–12.4 GHz (X-band) of AP/MBLM films with different LM weight ratios. **c** Average value of total shielding efficiency (SE_T), reflection shielding efficiency (SE_R), and absorption shielding efficiency (SE_A) of AP/MBLM films. Error bars represent standard deviations. **d** Average power coefficient of reflectivity (*R*), absorptivity (*A*), and transmissivity (*T*) of AP/MBLM and AP/MXene films. **e** Schematic diagram of the electromagnetic shielding mechanisms including the reflection of incident waves, conductance migration, internal multi-reflections, interfacial polarization and dipole polarization. **f** *EMI SE* curves of AP/MBLM11 films with different thicknesses. **g** Comparison of the theoretically calculated *SE* (SE_{theo}) based on Simon formulation and experimentally tested total *SE* (SE_T) of AP/MBLM11 nanocomposite film. Error bars represent standard deviations. **h** Comparison of the EMI shielding performance of AP/MBLM films with other recently reported EMI shielding materials (details can be found in Supplementary Fig. 19 and Supplementary Table 1).

tested total *EMI SE* (SE_T) values of the AP/MBLM11 film (Fig. 4g). The tested SE_T of the AP/MBLM film is constantly higher than the theoretically calculated SE_{theo} of a homogeneous shielding material at all thicknesses. Noticeably, with the increase in thickness, the value of ΔSE becomes larger, indicating that the inner dissipation effects are more pronounced in the thicker AP/MBLM film[58]. This observation substantiates the enhancement of *EMI SE* attributed to the inner dissipation effects generated by the layered heterogeneous structure of the AP/MBLM nanocomposite film. As a promising EMI shielding material the AP/MBLM film demonstrates superior EMI shielding performance compared to previously reported shielding materials filled with different conductive fillers (Fig. 4h, Supplementary Fig. 19 and Supplementary Table 1).

To validate the generality of the strategy, we replaced the MXene nanosheets with few-layer graphene sheets (GN) or graphene oxide nanosheets (GO) (Supplementary Fig. 20). AP/GNBLM and AP/rGOBLM films were fabricated using the same blade-casting, sol-gel-film conversion process, followed by the hot-pressing treatment. The cross-section morphology of the AP/MBLM, AP/GNBLM, and AP/rGOBLM film all demonstrate layered heterogeneous structure and the solid-liquid bi-continuous conductive networks can be observed (Supplementary Fig 21). The successful combination of GN, rGO, EGaIn LM and ANF in the AP/GNBLM film and AP/rGOBLM film can be confirmed through the investigation of XPS, XRD, and Raman spectra (see detailed discussion in Supplementary Fig. 22 and Supplementary Fig. 23). Interestingly an in-situ reduction of the GO nanosheets to rGO nanosheets during the mechanical sintering process was observed, which is in consistent with the reported articles[63,64]. This transformation leads to the change of AP/GO/SA@LM film to AP/rGOBLM film. The electrical conductance of the AP/GNBLM film and the AP/rGOBLM film demonstrate lower levels compared with AP/MBLM film (Supplementary Fig 24a). These discrepancies may be ascribed to the less densified bi-continuous conductive network caused by GN with inert surfaces[65], and the lower conductivity level caused by the limited

https://doi.org/10.1038/s41467-024-51732-9

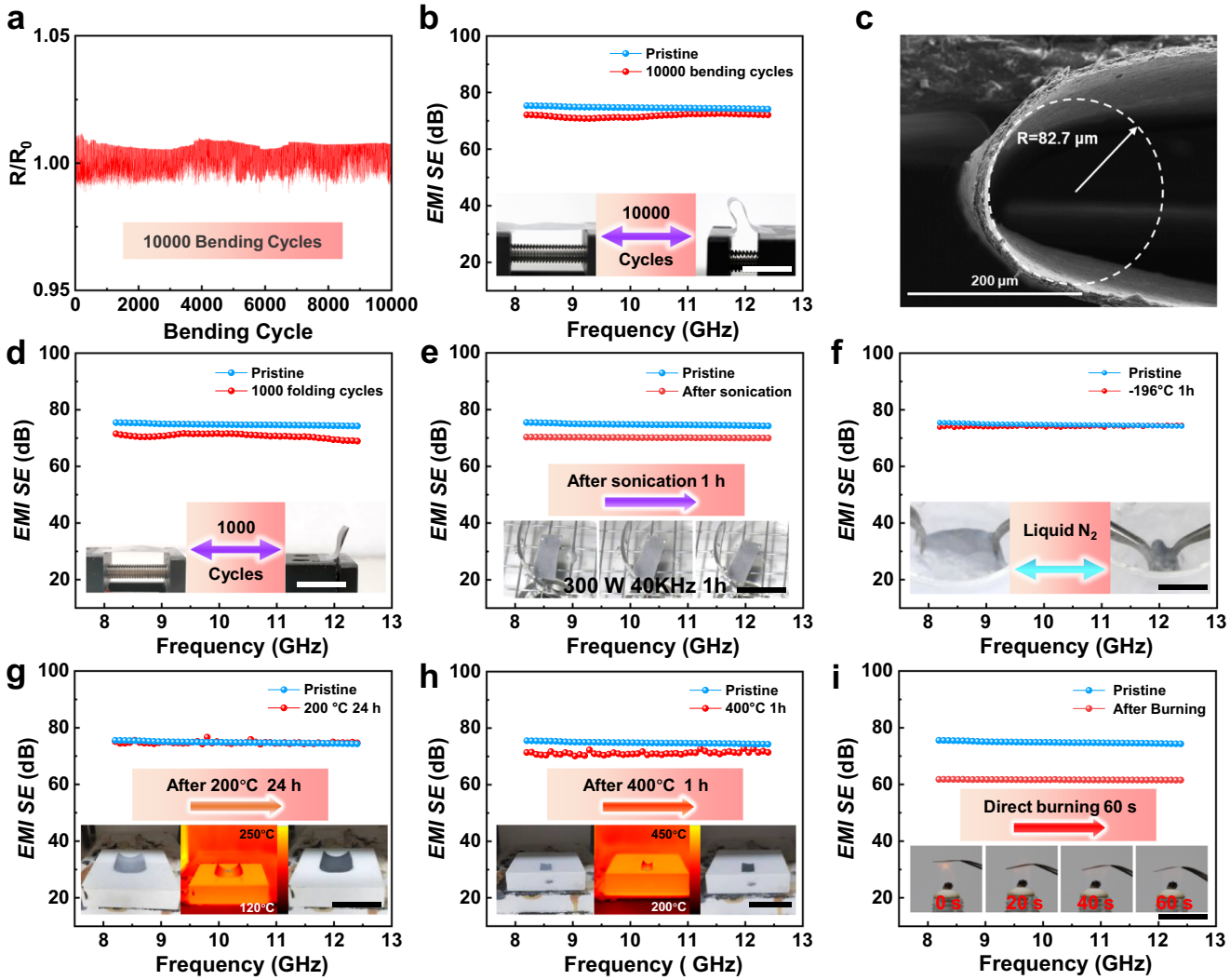

Fig. 5 | EMI shielding stability of AP/MBLM nanocomposite films after enduring harsh conditions. a The relative resistance variation of ANF/PVA (AP)/MXene-bridging-liquid metal (MBLM)11 film during 10000 bending cycles. **b** *EMI SE* of AP/MBLM11 film after 10000 bending cycles and the pristine one (scale bar: 2 cm). **c** SEM image of the cross-section of AP/MBLM11 film folding at a small radius of 82.7 μm. **d** *EMI SE* of the pristine AP/MBLM11 film and after 1000 folding cycles (scale bar: 2 cm). **e** *EMI SE* of AP/MBLM11 film after 300 W sonication for 1 h and the pristine one (scale bar: 3 cm). **f** *EMI SE* of AP/MBLM11 film after soaking in liquid nitrogen for 1 h and the pristine one (scale bar: 2 cm). **g** *EMI SE* of AP/MBLM11 film after 200 °C treatment for 24 h and the pristine one (scale bar: 5 cm). **h** *EMI SE* of AP/MBLM11 film after 400 °C treatment for 1 h and the pristine one (scale bar: 5 cm). **i** *EMI SE* of AP/MBLM11 film after direct burning for 1 min and the pristine one (scale bar: 4 cm).

reduction degree of rGO reduced by gallium[64], respectively. Although the electrical conductance of the AP/GNBLM film and AP/rGOBLM film can't reach the level comparable with the AP/MBLM film, they are still desirable for the application of EMI shielding. The variation in *EMI SE* of the AP/GNBLM film and AP/rGOBLM film is small over the entire X-band (Supplementary Fig. 24b). The SE_T of the AP/GNBLM film over the X-band frequency reached 64.5 dB at a thickness of 22 μm and the value of the AP/rGOBLM film reached 59.4 dB at a thickness of 22 μm (Supplementary Fig. 24c). These results demonstrate the universality of the strategy we proposed for constructing solid-liquid bi-continuous conductive networks with two-dimensional conductive nanosheets and EGaIn LM in ANF matrices, leading to the creation of nanocomposites with ultra-high electrical conductivity.

Enduring EMI shielding performance of the AP/MBLM nanocomposite film

The ability of materials to retain their EMI shielding efficiency after exposure to harsh conditions has become a crucial criterion for practical applications[24,51]. The resistance changes in response to bending is directly correlated with the durability of flexible EMI shielding materials. Benefiting from the fluidity and adhesiveness of LM, it adheres and welds the MXene nanosheets in a very stable manner, endowing great softness for the MBLM solid-liquid bi-continuous conductive network. Consequently, the AP/MBLM11 film shows a stable resistance change during 10000 bending cycles (Fig. 5a, Supplementary Movie 1). There is only a slight reduction in the *EMI SE* of the AP/MBLM11 film after the bending cycles, with the average *EMI SE* remaining approximately at 71.8 dB (Fig. 5b). After folding at a very small radius (folding radius = 82.7 μm) (Fig. 5c) for 1000 cycles (Supplementary Movie 2), the *EMI SE* of the AP/MBLM11 film only decreases to 70.7 dB (Fig. 5d). The *EMI SE* of the film remains above 70 dB even after 1 h ultrasonication at 300 W (Fig. 5e, Supplementary Movie 3). Overall, the AP/MBLM film demonstrates satisfying durability under mechanical wear, suggesting its potential application in routine scenarios. For the EMI protection of highly integrated electronic devices on aircraft or space shuttle in the domain of aeronautics and astronautics, the EMI shielding material may have to endure extreme temperatures[24]. Regarding the AP/MBLM film's tolerance to extremely

https://doi.org/10.1038/s41467-024-51732-9

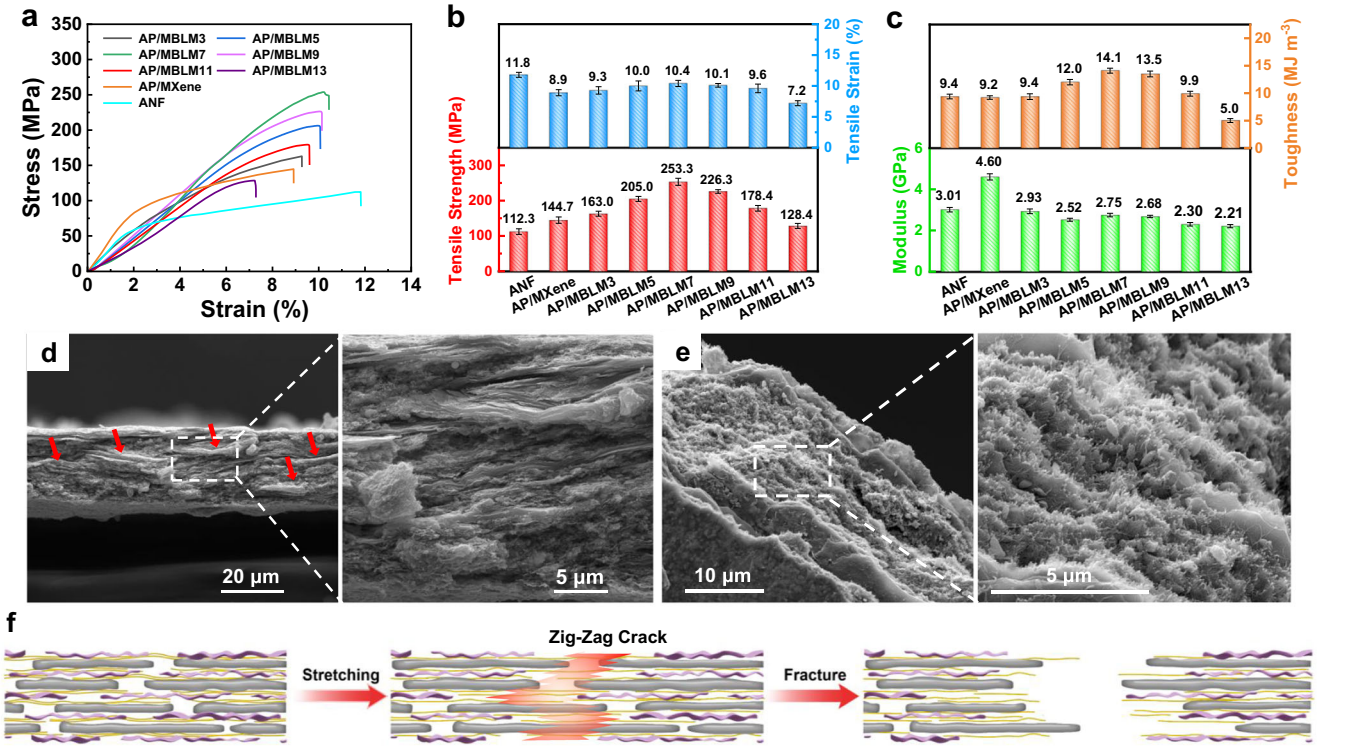

Fig. 6 | Mechanical properties of AP/MBLM nanocomposite films. a Typical stress-strain curves of ANF, ANF/PVA (AP)/MXene film, and AP/MXene-bridging-liquid metal (MBLM) films with different weight ratios. **b** Tensile strength and tensile strain of AP/MBLM films. **c** Toughness and modulus of AP/MBLM films. The error bars (**b**, **c**) represent the standard deviations. **d** Cross-section SEM image of the fracture behavior of AP/MBLM11 film, the red arrows indicate the "zig-zag" step-like crack regions. **e** Top-view SEM images of tensile fracture-surface morphologies of AP/MBLM11 film. f Schematic illustration of the fracture mechanism of AP/MBLM film.

low-temperature environments, cryogenic experiments were conducted using liquid nitrogen. As shown in Fig. 5f, the *EMI SE* of the AP/MBLM11 film shows no obvious decline after being soaked in liquid nitrogen for 1 h. The film even maintains good flexibility when soaked in liquid nitrogen (Supplementary Movie 4). This observation indicates that the AP/MBLM film maintains structural integrity and flexibility even after the crystallization of the LM lamellae (Supplementary Fig. 25). Verified by thermogravimetric analysis (TGA) (Supplementary Fig. 26), the AP/MBLM film exhibits good thermal stability. The high-temperature EMI shielding stability of the AP/MBLM film was examined through heat treatment in a Muffle furnace and subsequent testing (Supplementary Fig. 27 and Supplementary Fig. 28). As shown in Fig. 5g, h, the *EMI SE* of the AP/MBLM11 film remains almost unchanged after heat treatment at 200 °C for 24 h, and only a marginal decline is observed after heat treatment at 400 °C for 1 h. The detailed mechanisms behind this temperature-stable EMI shielding behavior are shown in Supplementary Figs. 29–31. In both circumstances, the *EMI SE* remained above 70 dB. These findings establish a broad operational temperature range of -196–400 °C for the AP/MBLM film as a temperature-stable EMI shielding material. The AP/MBLM11 film also demonstrates excellent fire retardance, maintaining a high *EMI SE* above 61 dB even after a 60 s direct exposure to the outer flame of an alcohol lamp (Fig. 5i, and Supplementary Movie 5). This behavior holds crucial significance for the insurance of the safety of electronic devices and electromagnetic protection under extremely harsh conditions[66].

Mechanical properties of AP/MBLM nanocomposite film

The structural robustness of the nanocomposite holds notable practical significance for its durability and reliability in applications under harsh conditions[13]. For instance, in the scenario of astronautics, a nanocomposite with high structural robustness may be applied to the outer shell of the spacecraft for EMI protection and thermal conduction. Figure 6a-c and Supplementary Fig. 32 show typical stress-strain curves and detailed mechanical properties of ANF, AP/MXene and AP/MBLM nanocomposite films. The stress-strain curve of the pure ANF film shows an elastic deformation at the initial tensile stage and then a long stretch of plastic deformation occurred, the ANF film shows a tensile strain of 11.8% and a tensile strength of 112.3 MPa. The Young's modulus and toughness of the ANF film is 3.01 GPa and 9.4 MJ/m^3, respectively. In contrast, the AP/MXene composite film demonstrates a significantly elevated Young's modulus and a higher tensile strength, measuring 4.60 GPa and 144.7 MPa, respectively. However, the tensile strain decreases to 8.9%. These results indicate a stiffer mechanical property of the AP/MXene film compared to the pure ANF film. This is attributed to the fill of rigid MXene nanosheets in the AP matrices, and the formation of hydrogen bonds between the MXene nanosheets, PVA short chains and ANF[67]. The introduction of the MBLM networks into the AP matrices has altered the shape of the stress-strain curve, prolonging the elastic deformation section. Despite a decrease in the modulus to 2.93 GPa for the AP/MBLM3 film, both tensile strength and tensile strain have increased to 163.0 MPa and 9.3%, respectively. This signifies a reinforcing effect of the MBLM networks on the resilience and elasticity of the nanocomposite film. The tensile strength of the nanocomposite film initially increases and then decreases with a further rise in MBLM content in the AP matrices. A similar trend is observed in the variation of tensile strain. The AP/MBLM7 film achieves a peak tensile strength of 253.3 MPa, a tensile strain of 10.4%, and a toughness of 14.1 MJ/m^3. Noticeably, despite the elevated MBLM network content in the AP/MBLM9 and AP/MBLM11 films, the tensile strength persists at a considerable level, reaching 226.3 MPa and 176.4 MPa, respectively. Whereas, with a further increase in the LM content of the AP/MBLM film, the mechanical strength of the sample

significantly declined due to the low fraction of AP matrices in the nanocomposite. For the comprehension of the reinforced mechanical properties of the nanocomposite films, the cross-section SEM images of the fractured AP/MBLM11 films were obtained. Following fracture, "zig-zag" step-like crack regions can be observed (Fig. 6d, red arrow). This fracture behavior is reminiscent of the natural structure of nacre, renowned for its efficacy in enhancing tensile resistance[68]. From a microscale perspective, during fracture events, cracks meander and penetrate deeply into the film's interior, as opposed to causing direct structural disruption by traversing it vertically[47]. This mechanism elucidates the dissipation of damaging energy, imparting a toughening effect. From a nanoscale perspective (Fig. 6e), the reinforcing mechanical strength is also achieved through the slip of MXene nanosheets, the extraction of the ANF@PVA nanofibers, and the deformation of soft LM lamellae. As depicted in Supplementary Fig. 33, hydrogen bonds formed among the PVA fibers, π-π stacking ANF chains, MXene nanosheets, and the broken SA shell adhered to the LM lamellae[45,46]. Moreover, the negatively charged oxygen-containing groups on SA chains and the MXene nanosheets generate electrostatic attraction forces with the positively charged oxide shell of LM[45,51]. Considering these interfacial interactions, the morphological changes mentioned above induce strong friction forces, preventing the plastic deformation of the nanocomposite film[30,46]. As depicted in Fig. 6f, during stretching, the MXene nanosheets, LM lamellae, and ANF@PVA nanofibers all endured a large deformation via a zig-zag crack propagation pathway before the final fracture. The microscale and nanoscale deformation synergistically contribute to the alternation in the shape of the stress-strain curves of the AP/MBLM films compared to the pure ANF film and AP/MXene film. The combination of these micro-nano hierarchical energy-dissipating interactions imparts the AP/MBLM film with robust and tough mechanical properties.

Thermal conductivity and heat-dissipation application

The heat accumulation in electronic devices always deteriorates their performance. For instance, the elevated working temperature of the central processing unit (CPU) substantially compromises its reliability and operational lifespan. This issue contributes to a notable 55% incidence of CPU failures[8]. To address this challenge, efficient heat dissipation in modern electronics with TIM is a crucial solution. In addition, the conversion of the EM waves into thermal energy is also an issue that should not be ignored for EMI shielding materials[26]. For these purposes, we systematically tested the thermal conductivity of the AP/MBLM films. As shown in Fig. 7a, the thermal conductivities of the AP/MBLM films exhibit a notable anisotropic property, with the in-plane thermal conductivity far beyond the through-plane thermal conductivity. Since the thickness of the AP/MBLM film is much smaller than its diameter, the through-plane thermal conductivity of the film in the thickness direction contributes minimally to cooling, whereas the in-plane thermal conductivity dominates efficient heat transfer[39,69,70]. This directional anisotropy in thermal conductivity is crucial for precise directional thermal management, allowing for efficient heat transfer to specific regions and providing better protection of highly integrated electronic equipment[39]. In comparison to the AP/MXene film, the thermal conductivities of the AP/MBLM films have been remarkably enhanced, with the AP/MBLM11 film achieving an in-plane thermal conductivity of 13.17 $W m^{-1} K^{-1}$, and the AP/MBLM13 film achieving a maximum in-plane thermal conductivity of 14.47 $W m^{-1} K^{-1}$. Additionally, the in-plane thermal conductivity of the AP/MBLM films remains relatively stable, with a marginal increase across different temperatures ranging from 25 °C to 200 °C (Fig. 7b). Similar to the AP/MBLM films, the thermal conductance of the AP/LM films also exhibit large anisotropy (Fig. 7c). Different from AP/MBLM films, the thermal conductivities of the AP/LM films without the bridging of MXene nanosheets are constantly lower than the values of AP/MBLM films, with the AP/LM13 film reaching a maximum value of only 8.65 $W m^{-1} K^{-1}$. The detailed thermal diffusivities of the samples are shown in Supplementary Tables 2–4. For the verification of the discrepancy in the thermal conductivity resulting from the introduction of MXene nanosheets, finite element simulations were conducted. The results, depicted in Fig. 7d, maintain the same 2D models as the simulations of electrical conductivity. In this simulation, a temperature of 80 °C is applied at the left boundary of the models. As the color transitions from orange-yellow to dark violet, there is a consistent and monotonic decrease in temperature. A pronounced color gradient indicates an increased thermal conducting resistance of the film. It is evident that the color gradient of the AP/MBLM film is smaller than that of the AP/LM film, and the right boundary temperature of the AP/MBLM film is higher than that of the AP/LM film (Supplementary Fig. 34). These results signify a higher thermal conductivity in the AP/MBLM film, consistent with the experimental findings. The thermal conducting mechanism is schematically illustrated in Fig. 7e, the oriented layered structure of the MBLM solid-liquid bi-continuous network creates fast transmission channels for heat conduction along the orientation direction. Whereas, heat conduction along the through-plane direction is hindered by cage effect of transversally arranged AP nanofibers. These mechanisms contribute to the observed anisotropic thermal conductivity[39,65]. Furthermore, the heat dissipation performance of the AP/MBLM nanocomposite film was studied by applying the film to the bottom of a lighting-emitting diode (LED) chip as heat-dissipating substrate (Fig. 7f). A thin layer of 0.2 g silicone thermal grease (DC 340 commercial silicone grease with a thermal conductivity of 0.67 $W m^{-1} K^{-1}$) was applied to ensure adequate contact between the AP/MBLM film and the bottom of the LED chip. To elucidate the heat-dissipating effect of the silicone grease, we also investigated the application of silicone grease alone without the heat-dissipating film. The real-time temperature data of the LED chip was obtained from infrared radiation (IR) images taken by an infrared camera (Fig. 7g). As illustrated in Fig. 7h, the central temperature of the bare LED chip without any heat-dissipating substrate reached 67.9 °C. The saturated temperature of the LED chip, coupled with silicone grease, reached 64.0 °C, showing a relatively limited heat dissipation behavior with a temperature decline of 3.9 °C. Conversely, the saturated temperature of the LED chip applied with the pure ANF film exhibited a slight decrease to 62.8 °C, indicating an almost negligible enhancement in heat dissipation behavior. In stark contrast, the saturated temperature of the LED chips coated with AP/MBLM films demonstrated much lower saturation temperatures and significantly higher cooling rates. For the LED chip coated with AP/MBLM11 film, the saturated temperature decreased by 14.2 °C, while the LED chip coated with AP/MBLM13 film showed an even greater drop in saturated temperature, with a decrease of 15.8 °C. These findings confirm that the AP/MBLM films offer significantly improved heat dissipation compared to commercial silicone thermal grease and pure ANF film. This underscores the considerable potential of AP/MBLM films in serving as TIM.

Discussion

In this work, we introduced a universal strategy for constructing solid-liquid thermal/electrical bi-continuous conductive networks in the ANF matrix. The as-prepared ultrathin AP/MBLM film exhibits ultra-high electrical conductivity of 3984 S/cm. Consequently, the AP/MBLM film demonstrates a promising *EMI SE* of 74.6 dB, ultra-high *EMI SSE* per unit thickness of 4950 dB/mm. The sophisticated interactions including hydrogen bonds and electrostatic interactions among the polymer contents and the MBLM networks contribute to a reinforced mechanical property (tensile strength of 253.3 MPa, tensile strain of 10.4%, and toughness of 14.1 MJ/m^3). Furthermore, the AP/MBLM film also demonstrates high in-plane thermal conductivity, reaching up to 14.47 $W m^{-1} K^{-1}$, and effective heat dissipating performance. Combining excellent electrical and thermal conductivity with promising flexibility and durability, the AP/MBLM nanocomposite films are poised to

https://doi.org/10.1038/s41467-024-51732-9

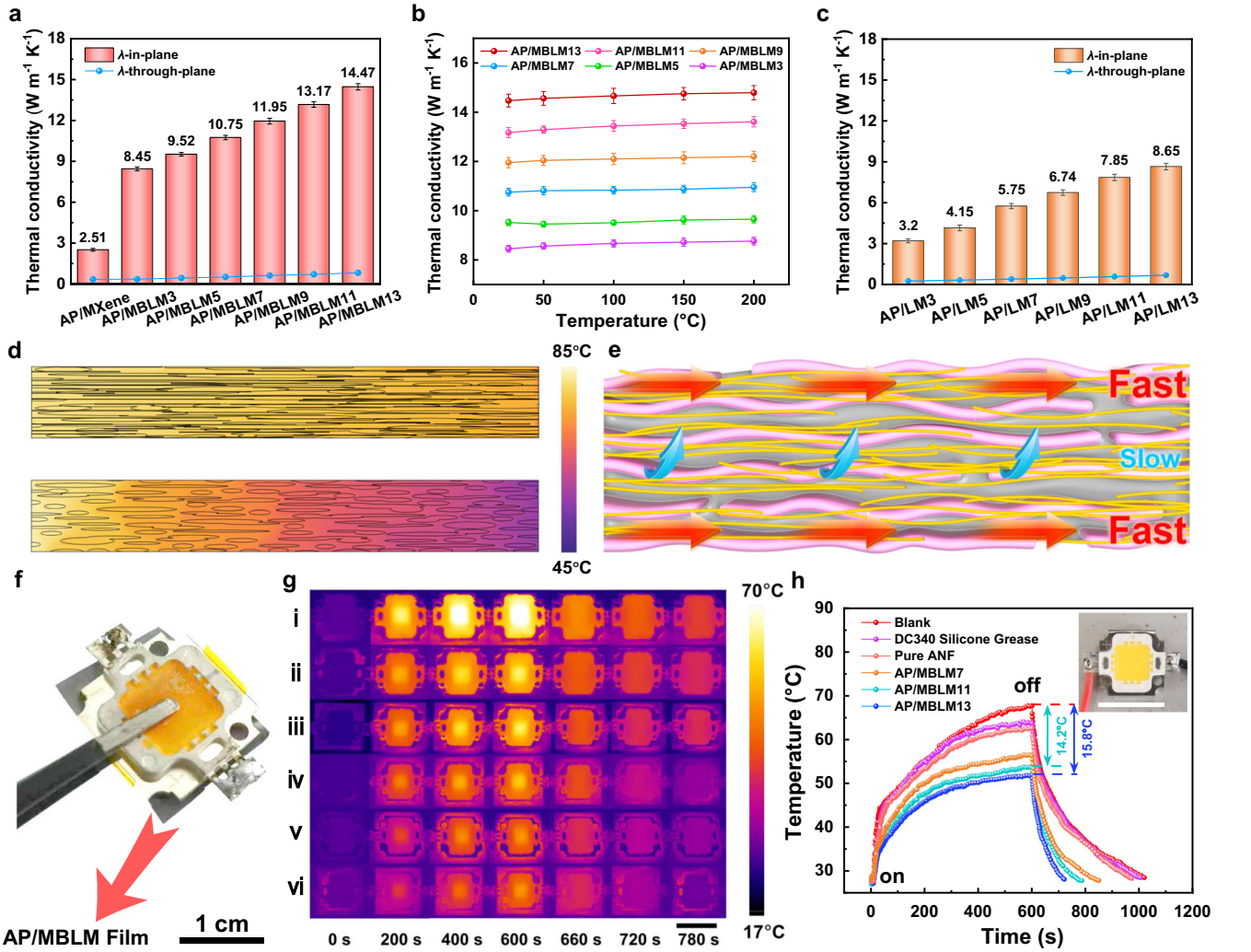

Fig. 7 | Thermal conductivity and heat-dissipating performance of AP/MBLM nanocomposite film. a Thermal conductivity of ANF/PVA (AP)/MXene-bridging-liquid metal (MBLM) films with different weight ratios. **b** In-plane thermal conductivity of AP/MBLM films with different weight ratios at different environmental temperatures. **c** Thermal conductivity of AP/LM films with different weight ratios. The error bars (**a**–**c**) represent the standard deviations. **d** Finite element simulation results of in-plane directional temperature distribution of AP/MBLM film. **e** Schematic diagram of the mechanism for thermal conduction in AP/MBLM nanocomposite film (the large red arrows indicate high in-plane thermal conductivity, while the small blue arrows indicate slow through-plane thermal conductivity of the AP/MBLM films). **f** Optical image of an LED chip coupled with an AP/MBLM film as a heat spreader. **g** IR thermal images of the LED chip operating under 24 V without heat spreader (i), coupled with (ii) DC340 silicone thermal grease, and thermal grease glued substrates of (iii) pure ANF film, (iv) AP/MBLM7 film and (v) AP/MBLM11 film, and (vi) AP/MBLM13 film, scale bar: 2 cm. **h** corresponding temperature-time relationship curves, scale bar: 2 cm.

revolutionize EMI shielding and thermal management in the next-generation electronics. Their exceptional performance carries significant potential for advancements in flexible electronics, defense equipment, and aeronautics and astronautics.

Methods

General information

For raw materials, fabrication procedures of ANF@PVA/DMSO dispersion, $Ti_3C_2T_x$ MXene nanosheets and MXene/DMSO dispersion, SA@LM/DMSO nano-emulsion, GN/DMSO dispersion, GO/DMSO dispersion, material characterization, measurement of EMI shielding performance, and finite element simulation, see Supplementary Methods.

Preparation of AP/MBLM nanocomposite film. The AP/MBLM nanocomposite film was prepared via a sol-gel-film conversion approach and following hot compression. The details are as follows: Initially, 15 g of AP/DMSO dispersion was combined with 10 ml of MXene/DMSO dispersion and magnetically stirred for 30 min, and the weight ratio of MXene to AP matrices was fixed at 1:2. Following this, 10 ml of SA@LM/DMSO nano-emulsion with different LM mass concentration was added, and the mixture was stirred for an additional 2 h to form the casting solution. Subsequently, the casting solution was blade-coated on a PET substrate and immersed in DI water for reprotonation, resulting in the formation of the hydrogel. Afterward, the hydrogel was transferred into a mixture of tert-butylalcohol and DI water with a mass ratio of 1:1 for extraction for 24 h. The hydrogel was then evaporated in air at 45 °C to form the AP/MXene/SA@LM heterogeneous film. Ultimately, the film was hot-pressed at 70 °C and 30 MPa to obtain the AP/MBLM nanocomposite film. A series of AP/MBLM films with varying LM to AP weight ratios of 3:1, 5:1, 7:1, 9:1, 11:1, and 13:1were prepared by adjusting the LM mass concentration in the SA@LM nano-emulsion. These films are labeled as AP/MBLM3, AP/MBLM5, AP/MBLM7, AP/MBLM9, AP/MBLM11 and AP/MBLM13, respectively.

Preparation of AP/LM nanocomposite film. 15 g of AP/DMSO dispersion was combined with 10 ml of SA@LM/DMSO nano-emulsion

with different LM mass concentrations. After magnetic stirring for 2 h, the resulting dispersion was blade-cast onto a PET substrate and promptly immersed in DI water to create an AP/SA@LM hydrogel. Subsequently, the hydrogel underwent extraction in a mixture of tert-butyl alcohol and DI water with a mass ratio of 1:1 for 24 h. The hydrogel was then evaporated in air at 45 °C, followed by hot pressing at 70 °C and 30 MPa, obtaining the AP/LM film. A set of AP/LM films with different LM to AP weight ratios (3:1, 5:1, 7:1, 9:1, 11:1, and 13:1) were fabricated by modifying the LM mass concentration in the SA@LM nano-emulsion. These films are denoted as AP/LM3, AP/LM5, AP/LM7, AP/LM9, AP/LM11, and AP/LM13 respectively.

Preparation of AP/GNBLM nanocomposite film. 15 g of AP/DMSO dispersion was combined with 10 ml of GN/DMSO dispersion and magnetically stirred for 30 min, the weight ratio of GN to AP matrices was fixed at 1:2. Subsequently, 10 ml of SA@LM/DMSO nano-emulsion with a LM mass concentration of 330 mg/ml was added, and the mixture was stirred for an additional 2 h to form the casting solution. The following preparation process stays the same with the AP/MBLM nanocomposite film.

Preparation of AP/rGOBLM nanocomposite film. 15 g of AP/DMSO dispersion was combined with 10 ml of GO/DMSO dispersion and magnetically stirred for 30 min, the weight ratio of GO to AP matrices was fixed at 1:2. Subsequently, 10 ml of SA@LM/DMSO nano-emulsion with a LM mass concentration of 330 mg/ml was added, and the mixture was stirred for an additional 2 h to form the casting dispersion. The dispersion was blade-cast onto a PET substrate and promptly immersed in DI water to create an AP/GO/SA@LM hydrogel. Subsequently, the hydrogel underwent extraction in a mixture of tert-butyl alcohol and DI water with a mass ratio of 1:1 for 24 h. The hydrogel was then evaporated in the air at 45 °C to form the AP/GO/SA@LM heterogeneous film, followed by hot pressing at 70 °C and 30 MPa, obtaining the AP/rGOBLM film.

Calculation of the theoretical EMI SE of the AP/MBLM film. The theoretical EMI SE of the AP/MBLM nanocomposite film is calculated based on Simon's formulation as follow:

$$SE_T = 50 + 10\lg(\sigma/f) + 1.7t\sqrt{\sigma f} \quad (1)$$

Where σ represents the electrical conductivity (S/cm) of the material, f represents the frequency of the EM field (MHz), and t represents the thickness of the material (cm).

Data availability

The authors declare that data supporting the findings of this study are available within the paper and its Supplementary Information Files. Data are also available from the corresponding author upon request. Source data are provided with this paper.

References

1. Conti, S. et al. Printed transistors made of 2D material-based inks. *Nat. Rev. Mater.* **8**, 651–667 (2023).
2. Chen, Z., Xu, C., Ma, C., Ren, W. & Cheng, H.-M. Lightweight and flexible graphene foam composites for high-performance electromagnetic interference shielding. *Adv. Mater.* **25**, 1296–1300 (2013).
3. Shahzad, F. et al. Electromagnetic interference shielding with 2D transition metal carbides (MXenes). *Science* **353**, 1137–1140 (2016).
4. Iqbal, A. et al. Anomalous absorption of electromagnetic waves by 2D transition metal carbonitride Ti_3CNT_x (MXene). *Science* **369**, 446–450 (2020).
5. Hashemi, S. A. et al. Recent progress on hybrid fibrous electromagnetic shields: Key protectors of living species against electromagnetic radiation. *Matter* **5**, 3807–3868 (2022).
6. Moore, A. L. & Shi, L. Emerging challenges and materials for thermal management of electronics. *Mater. Today* **17**, 163–174 (2014).
7. Qian, X., Zhou, J. & Chen, G. Phonon-engineered extreme thermal conductivity materials. *Nat. Mater.* **20**, 1188–1202 (2021).
8. Qin, B. & Zhao, L.-D. Moving fast makes for better cooling. *Science* **378**, 832–833 (2022).
9. Sun, W. et al. Performance optimization of a dual-thermoelectric-liquid hybrid system for central processing unit cooling. *Energy Convers. Manag.* **290**, 117222 (2023).
10. Xie, Z., Avila, R., Huang, Y. & Rogers, J. A. Flexible and stretchable antennas for biointegrated electronics. *Adv. Mater.* **32**, 1902767 (2020).
11. Lim, H.-R. et al. Advanced soft materials, sensor integrations, and applications of wearable flexible hybrid electronics in healthcare, energy, and environment. *Adv. Mater.* **32**, 1901924 (2020).
12. Li, J., Liu, X., Feng, Y. & Yin, J. Recent progress in polymer/two-dimensional nanosheets composites with novel performances. *Prog. Polym. Sci.* **126**, 101505 (2022).
13. Liang, C., Qiu, H., Zhang, Y., Liu, Y. & Gu, J. External field-assisted techniques for polymer matrix composites with electromagnetic interference shielding. *Sci. Bull.* **68**, 1938–1953 (2023).
14. Xu, X. F., Zhou, J. & Chen, J. Thermal transport in conductive polymer-based materials. *Adv. Funct. Mater.* **30**, 1904704 (2020).
15. Ji, H. et al. Lightweight and flexible electrospun polymer nanofiber/metal nanoparticle hybrid membrane for high-performance electromagnetic interference shielding. *NPG Asia Mater.* **10**, 749–760 (2018).
16. Ma, Z. et al. High-performance and rapid-response electrical heaters based on ultraflexible, heat-resistant, and mechanically strong aramid nanofiber/Ag nanowire nanocomposite papers. *ACS Nano* **13**, 7578–7590 (2019).
17. Shin, B. et al. Flexible thermoplastic polyurethane-carbon nanotube composites for electromagnetic interference shielding and thermal management. *Chem. Eng. J.* **418**, 129282 (2021).
18. Fu, C., Sheng, Z. & Zhang, X. Laminated structural engineering strategy toward carbon nanotube-based aerogel films. *ACS Nano* **16**, 9378–9388 (2022).
19. Huang, L. et al. Self-exfoliation of flake graphite for bioinspired compositing with aramid nanofiber toward integration of mechanical and thermoconductive properties. *Nano-Micro Lett.* **14**, 168 (2022).
20. Wei, Q. et al. Scalable fabrication of nacre-structured graphene/polytetrafluoroethylene films for outstanding EMI shielding under extreme environment. *Small* **19**, 2302082 (2023).
21. Wei, Q. et al. Superhigh electromagnetic interference shielding of ultrathin aligned pristine graphene nanosheets film. *Adv. Mater.* **32**, 1907411 (2020).
22. Li, L. et al. Flexible and ultrathin graphene/aramid nanofiber carbonizing films with nacre-like structures for heat-conducting electromagnetic wave shielding/absorption. *ACS Appl Mater. Interfaces* **15**, 15872–15883 (2023).
23. Ma, Z. et al. Ultraflexible and mechanically strong double-layered aramid nanofiber–$Ti_3C_2T_x$ MXene/silver nanowire nanocomposite papers for high-performance electromagnetic interference shielding. *ACS Nano* **14**, 8368–8382 (2020).
24. Cheng, Y. et al. Hierarchically porous polyimide/$Ti_3C_2T_x$ film with stable electromagnetic interference shielding after resisting harsh conditions. *Sci. Adv.* **7**, eabj1663 (2021).
25. Wang, J., Ma, X., Zhou, J., Du, F. & Teng, C. Bioinspired, high-strength, and flexible MXene/aramid fiber for electromagnetic interference shielding papers with joule heating performance. *ACS Nano* **16**, 6700–6711 (2022).
26. Zhang, Y. L., Ruan, K. P., Zhou, K. & Gu, J. W. Controlled distributed $Ti_3C_2T_x$ hollow microspheres on thermally conductive polyimide

composite films for excellent electromagnetic interference shielding. *Adv. Mater.* **35**, 2211642 (2023).
27. Yin, G. et al. Dynamic adaptive wrinkle-structured silk fibroin/MXene composite fibers for switchable electromagnetic interference shielding. *Adv Funct Mater*. 2314425 https://doi.org/10.1002/adfm.202314425 (2024).
28. VahidMohammadi, A., Rosen, J. & Gogotsi, Y. The world of two-dimensional carbides and nitrides (MXenes). *Science* **372**, eabf1581 (2021).
29. Wang, W.-Y. et al. Flexible, multifunctional, and thermally conductive nylon/graphene nanoplatelet composite papers with excellent EMI shielding performance, improved hydrophobicity and flame resistance. *J. Mater. Chem. A* **9**, 5033–5044 (2021).
30. Liao, S.-Y. et al. Flexible liquid metal/cellulose nanofiber composites film with excellent thermal reliability for highly efficient and broadband EMI shielding. *Chem. Eng. J.* **422**, 129962 (2021).
31. Wan, Y. et al. Ultrathin, strong, and highly flexible $Ti_3C_2T_x$ MXene/bacterial cellulose composite films for high-performance electromagnetic interference shielding. *ACS Nano* **15**, 8439–8449 (2021).
32. Cheng, J. Y. et al. Recent advances in design strategies and multifunctionality of flexible electromagnetic interference shielding materials. *Nano-Micro Lett.* **14**, 80 (2022). 14.
33. Liu, C. et al. Enhanced electromagnetic shielding and thermal management properties in MXene/aramid nanofiber films fabricated by intermittent filtration. *ACS Appl Mater. Interfaces* **15**, 4516–4526 (2023).
34. Liu, Y., Zhao, N. & Xu, J. Mechanically strong and flame-retardant PBO/BN/MXene nanocomposite paper with low thermal expansion coefficient, for efficient EMI shielding and heat dissipation. *Adv. Fiber Mater.* **5**, 1657–1670 (2023).
35. Yang, M. et al. Dispersions of aramid nanofibers: A new nanoscale building block. *ACS Nano* **5**, 6945–6954 (2011).
36. He, A. et al. Advanced aramid fibrous materials: Fundamentals, advances, and beyond. *Adv. Fiber Mater.* **6**, 3–35 (2024).
37. Zhao, B., Ma, Z., Sun, Y., Han, Y. & Gu, J. Flexible and robust $Ti_3C_2T_x$/(ANF@FeNi) composite films with outstanding electromagnetic interference shielding and electrothermal conversion performances. *Small Struct.* **3**, 2200162 (2022).
38. Yang, L. et al. Revealing the interrelation between hydrogen bonds and interfaces in graphene/PVA composites towards highly electrical conductivity. *Chem. Eng. J.* **383**, 123126 (2020).
39. Liu, Y., Zou, W., Zhao, N. & Xu, J. Electrically insulating PBO/MXene film with superior thermal conductivity, mechanical properties, thermal stability, and flame retardancy. *Nat. Commun.* **14**, 5342 (2023).
40. Ma, J. et al. Shaping a soft future: Patterning liquid metals. *Adv. Mater.* **35**, 2205196 (2023).
41. Xiang, W. et al. Liquid-metal-based magnetic fluids. *Nat Rev Mater.* **9**, 433–449 (2024).
42. Zhou, X. et al. Biphasic gain alloy constructed stable percolation network in polymer composites over ultrabroad temperature region. *Adv. Mater.* **36**, 2310849 (2024).
43. Ma, Z. et al. Permeable superelastic liquid-metal fibre mat enables biocompatible and monolithic stretchable electronics. *Nat. Mater.* **20**, 859–868 (2021).
44. Li, X. K. et al. Liquid metal droplets wrapped with polysaccharide microgel as biocompatible aqueous ink for flexible conductive devices. *Adv. Funct. Mater.* **28**, 1804197 (2018).
45. Che, X. P. et al. Two-dimensionally nano-capsulating liquid metal for self-sintering and self-oscillating bimorph composites with persistent energy-harvest property. *Adv Funct. Mater.* **34**, 2307830 (2024).
46. Zhou, T. et al. Large-area ultrastrong and stiff layered MXene nanocomposites by shear-flow-induced alignment of nanosheets. *ACS Nano* **16**, 12013–12023 (2022).
47. Jin, J. et al. A synergistic interfacial and topological strategy for reinforcing aramid nanofiber films. *Mater. Horiz.* **10**, 4626–4634 (2023).
48. Hu, P. et al. Multifunctional aramid nanofiber/carbon nanotube hybrid aerogel films. *ACS Nano* **14**, 688–697 (2020).
49. Li, X. et al. Evaporation-induced sintering of liquid metal droplets with biological nanofibrils for flexible conductivity and responsive actuation. *Nat. Commun.* **10**, 3514 (2019).
50. Qi, X. et al. Versatile liquid metal/alginate composite fibers with enhanced flame retardancy and triboelectric performance for smart wearable textiles. *Adv. Sci.* **10**, 2303406 (2023).
51. Sun, Y. et al. Slippery graphene-bridging liquid metal layered heterostructure nanocomposite for stable high-performance electromagnetic interference shielding. *ACS Nano* **17**, 12616–12628 (2023).
52. Zhang, J. Z. et al. Scalable manufacturing of free-standing, strong $Ti_3C_2T_x$ MXene films with outstanding conductivity. *Adv. Mater.* **32**, 2001093 (2020).
53. Wang, C. H. et al. A general approach to composites containing nonmetallic fillers and liquid gallium. *Sci. Adv.* **7**, eabe3767 (2021).
54. Zhu, R. et al. Anisotropic magnetic liquid metal film for wearable wireless electromagnetic sensing and smart electromagnetic interference shielding. *Nano Energy* **92**, 106700 (2022).
55. Han, M. et al. Beyond $Ti_3C_2T_x$: MXenes for electromagnetic interference shielding. *ACS Nano* **14**, 5008–5016 (2020).
56. Toker, D., Azulay, D., Shimoni, N., Balberg, I. & Millo, O. Tunneling and percolation in metal-insulator composite materials. *Phys. Rev. B* **68**, 041403 (2003).
57. Peng, M. & Qin, F. Clarification of basic concepts for electromagnetic interference shielding effectiveness. *J. Appl Phys.* **130**, 225108 (2021).
58. Li, B. et al. Bicontinuous, high-strength, and multifunctional chemical-cross-linked MXene/superaligned carbon nanotube film. *ACS Nano* **16**, 19293–19304 (2022).
59. Lv, H. L. et al. Staggered circular nanoporous graphene converts electromagnetic waves into electricity. *Nat. Commun.* **14**, 1982 (2023).
60. Yi, P. et al. MXene-reinforced liquid metal/polymer fibers via interface engineering for wearable multifunctional textiles. *ACS Nano* **16**, 14490–14502 (2022).
61. Yousefi, N. et al. Highly aligned graphene/polymer nanocomposites with excellent dielectric properties for high-performance electromagnetic interference shielding. *Adv. Mater.* **26**, 5480–5487 (2014).
62. He, X. et al. High-performance multifunctional carbon–silicon carbide composites with strengthened reduced graphene oxide. *ACS Nano* **15**, 2880–2892 (2021).
63. Zhang, Y. et al. Synthesis of liquid gallium@reduced graphene oxide core–shell nanoparticles with enhanced photoacoustic and photothermal performance. *J. Am. Chem. Soc.* **144**, 6779–6790 (2022).
64. Baharfar, M. et al. Exploring interfacial graphene oxide reduction by liquid metals: Application in selective biosensing. *ACS Nano* **15**, 19661–19671 (2021).
65. Zhang, X. et al. Nerve-fiber-inspired construction of 3D graphene "tracks" supported by wood fibers for multifunctional biocomposite with metal-level thermal conductivity. *Adv. Funct. Mater.* **33**, 2213274 (2023).
66. Jin, X. et al. Flame-retardant poly(vinyl alcohol)/MXene multilayered films with outstanding electromagnetic interference shielding and thermal conductive performances. *Chem. Eng. J.* **380**, 122475 (2020).
67. Nie, Z. et al. Large-area ultrastrong and stiff aramid nanofiber based layered nanocomposite films. *Nano Res* **17**, 829–835 (2024).
68. Tang, Z., Kotov, N. A., Magonov, S. & Ozturk, B. Nanostructured artificial nacre. *Nat. Mater.* **2**, 413–418 (2003).

69. Chen, Q. et al. Scalable, robust, low-cost, and highly thermally conductive anisotropic nanocomposite films for safe and efficient thermal management. *Adv. Funct. Mater.* **32**, 2110782 (2022).
70. Xin, G. et al. Large-area freestanding graphene paper for superior thermal management. *Adv. Mater.* **26**, 4521–4526 (2014).

Acknowledgements

We gratefully acknowledge support from the National Natural Science Foundation of China (No. 52273101, 51922018, 21875011) (L.-P.H.).

Author contributions

Y.S. and L.-P.H. conceived this project and wrote and revised the manuscript. Y.S., Y.-T.S., Z.-Y.C. performed the experiments and characterizations. Y.S. conducted the finite element simulation. L.-P.H. and L.J. supervised the project. All authors discussed the results and commented on the manuscript.

Competing interests

The authors declare no competing interests.

Additional information

Supplementary information The online version contains supplementary material available at https://doi.org/10.1038/s41467-024-51732-9.

Correspondence and requests for materials should be addressed to Liping Heng.

Peer review information *Nature Communications* thanks Junye Cheng and Baowen Li for their contribution to the peer review of this work. A peer review file is available.